

## CFD-FSI simulation of vortex-induced vibrations of a circular cylinder with low mass-damping

Amir Borna<sup>\*1</sup>, Wagdi G. Habashi<sup>1</sup>, Ghyslaine McClure<sup>2</sup> and Siva K. Nadarajah<sup>1</sup>

<sup>1</sup>Computational Fluid Dynamics Laboratory, Department of Mechanical Engineering,  
McGill University, Montreal, QC, Canada H3A 2S6

<sup>2</sup>Department of Civil Engineering and Applied Mechanics,  
McGill University, Montreal, QC, Canada H3A 2S6

(Received February 25, 2012, Revised June 13, 2012, Accepted June 20, 2012)

**Abstract.** A computational study of vortex-induced transverse vibrations of a cylinder with low mass-damping is presented. An Arbitrary Lagrangian-Eulerian (ALE) formulation of the Unsteady Reynolds-Averaged Navier-Stokes equations (URANS), along with the Spalart-Allmaras (SA) one-equation turbulence model, are coupled conservatively with rigid body motion equations of the cylinder mounted on elastic supports in order to study the amplitude and frequency response of a freely vibrating cylinder, its flow-induced motion, Vortex Street, near-wake flow structure, and unsteady loading in a moderate range of Reynolds numbers. The time accurate response of the cylinder from rest to its limit cycle is studied to explore the effects of Reynolds number on the start of large displacements, motion amplitude, and frequency. The computational results are compared with published physical experiments and numerical studies. The maximum amplitudes of displacements computed for various Reynolds numbers are smaller than the experimental values; however, the overall agreement of the results is quite satisfactory, and the upper branch of the limit-cycle displacement amplitude vs. reduced velocity response is captured, a feature that was missed by other studies. Vortex shedding modes, lock-in phenomena, frequency response, and phase angles are also in agreement with experiments.

**Keywords:** vortex-induced vibrations; URANS; fluid-structure interaction; low mass-damping; turbulent flows

### 1. Introduction

Interactions of fluid and bluff bodies of cylindrical shape occur in many engineering applications such as overhead transmission lines, marine cables, flexible risers, suspended and cable-stayed bridges and chimneys. In these examples, vortex shedding behind the bluff body induces vibrations ranging from small to very large amplitudes. This kind of fluid-structure interaction (FSI) is known as vortex-induced vibrations (VIV). Different aspects of VIV, including vortex dynamics in the wake, lock-in phenomena, lift and drag measurements, have been extensively studied experimentally, and comprehensive reviews have been published during the past decades, see e.g., (Feng 1968, Sarpkaya 1979, Bearman 1984, Blevins 1994, Khalak *et al.*

---

\*Corresponding author, PhD candidate, E-mail: [amir.borna@mail.mcgill.ca](mailto:amir.borna@mail.mcgill.ca)

1996, Blackburn *et al.* 2001, Sarpkaya 2004, Williamson *et al.* 2004). However, the shortage of knowledge to explain certain observed features of fluid-bluff-body interactions, and the adverse effects of VIV in engineering applications such as structural instabilities, fatigue, severe damage, and infrastructural failure, keep VIV a challenging research area. More research is ongoing to understand the fundamental characteristics of VIV in order to prevent or control destructive vibrations and provide design guidelines. Finally, the large computational resources and long simulation durations required to study VIV numerically make it interesting to develop cost and time effective methodologies suitable for industrial applications.

The case of a freely vibrating smooth cylinder is fundamental to the study of VIV, and its reliable experimental studies make it an interesting benchmark for numerical validations. The experiments of Govardhan *et al.* (2000) show that the response of a freely oscillating cylinder with low mass-damping ratio in a transverse direction includes three distinct branches; “initial excitation”, then “upper”, and finally “lower” branches. At high mass ratio, the “upper” branch is absent, as indicated in (Feng 1968). Along with such experimental studies, few numerical studies have explored VIV and the response branches. Blackburn *et al.* (1993) used a spectral element method to study a forced and freely vibrating cylinder at Re 200 with low mass-damping, while Newman *et al.* (1997) performed a direct numerical simulation (DNS) to study a freely vibrating cable at Re 200, with no damping. In both studies, a maximum displacement of 0.65 is reported. Few other DNS studies has been reported in the literature (Blackburn *et al.* 2001, Williamson *et al.* 2004); however, all studies are done for low Reynolds numbers, ranging from 100 to 1000. These Reynolds numbers are much smaller than the actual Reynolds numbers encountered in real infrastructure engineering applications. The large computational demands of DNS calculations and their stability issues prevent extending these methods to higher Reynolds and/or three-dimensional industrial cases. Large eddy simulations (LES) are also not affordable because of the large simulation times required for VIV computations. Thus, Reynolds-Averaged Navier-Stokes (RANS) simulations are currently acceptable alternatives for industrial applications and provide adequate engineering accuracy. In spite of these advantages, there are few published RANS studies of VIV.

Guilmineau *et al.* (2004) performed a RANS simulation with the shear-stress transport (SST)  $k-\omega$  turbulence model for a Reynolds range of 1000-15000. In their study, different initial conditions are applied in order to predict the maximum amplitude observed in experiments and explore the hysteresis response of a cylinder. Although, according to the initial conditions used, they predicted the maximum amplitude close to the experiment; their results show some discrepancy in predicting the upper response branch. A similar numerical study has been done by Pan *et al.* (2007) in order to investigate discrepancies between the RANS model and experiment. They suggested that the response in the upper branch may be related to “intermittent switching” between the two other branches (lower and initial) in which the vortex shedding mode changes from 2S to 2P. They concluded that the formation of the upper branch is related to random physical disturbances when switching between 2P and 2S modes, which are not accounted for in RANS models. Recently, Pomarède *et al.* (2010) studied the transverse vibrations of a cylinder using a fully coupled FSI scheme, without damping and at low Reynolds numbers.

This paper presents a computational study of the vortex-induced cross flow oscillations of a cylinder with low mass-damping ratio at moderate Reynolds numbers. The computational method proposed is both cost and time effective, while maintaining accuracy. The following salient analysis features are presented: time accurate evolution of vortices, accuracy of the model in predicting structural response, near-wake flow structure, shedding frequency, unsteady fluid loading, and interpretation of the structural response. This study is aimed as a first step in the

numerical validation of a comprehensive computational fluid-structure interaction analysis framework for the study of structural instabilities in transmission line conductors subject to wind loads and atmospheric icing.

## 2. Governing equations and solution algorithm

### 2.1 Fluid dynamics

The URANS equations are solved using FENSAP-ICE, a second order accurate 3D finite element compressible Navier-Stokes solver (Habashi *et al.* 2004, Habashi 2009). In order to handle the moving nodes on the fluid/structure boundary and determine the new positions of the internal nodes in the fluid domain, an Arbitrary Lagrangian Eulerian (ALE) formulation is applied. The non-dimensional URANS equations used in FENSAP-ICE can be expressed as

$$\frac{\partial \rho}{\partial t} - \bar{u}_i \rho_{,i} + (\rho u_i)_{,i} = 0, \quad (1)$$

$$\frac{\partial \rho u_i}{\partial t} - \bar{u}_i (\rho u_i)_{,i} + (\rho u_i u_j)_{,j} = -p_{,i} + \text{Re}_\infty^{-1} \tau_{ij,j} - (\overline{\rho u_i u_j})_{,j}, \quad (2)$$

where  $\rho$  is the density,  $t$  time,  $u_i$  the  $i^{\text{th}}$  component of the velocity,  $\bar{u}_i$  the mesh velocity,  $p$  the pressure,  $\tau$  the stress tensor,  $\text{Re}_\infty$  the free stream Reynolds number, and  $\overline{\rho u_i u_j}$  the Reynolds stress tensor. The one-equation Spalart-Allmaras turbulence model of Spalart *et al.* (1992) is applied to estimate the Reynolds stress tensor.

### 2.2 Rigid body dynamics

The vertical motion of the rigid cylinder can be represented by a viscously damped linear single degree-of-freedom system with the following classical equation

$$m\ddot{y} + c\dot{y} + ky = F_y, \quad (3)$$

where  $y$  is the transverse displacement,  $m$  the cylinder mass,  $c$  the structural viscous damping,  $k$  the stiffness, and  $F_y$  the fluid loading resulting from the fluid surface loads. A non-dimensional form of this equation is obtained as follows, where the displacement is normalized with respect to the diameter of the cylinder

$$\frac{d^2 Y}{d\tau^2} + 4\pi \bar{f}_n \zeta \frac{dY}{d\tau} + (2\pi \bar{f}_n)^2 Y = \frac{4}{m^* \pi} C_L, \quad (4)$$

where  $\zeta$  is the structural viscous damping ratio,  $\bar{f}_n$ , the natural frequency,  $m^*$ , the mass ratio, and  $C_L$  the unsteady lift coefficient. The normalized variables used in Eq. (4), and other normalized variables used throughout the text, are defined as following:

$$\begin{aligned}
Y = y/D, \quad \tau = tU_\infty/D, \quad m^* = \frac{m}{m_d}, \quad m_d = \frac{\pi}{4} \rho D^2, \\
U^* = \frac{U_\infty}{f_n D}, \quad C_L = \frac{F_y}{\rho U_\infty^2 D}, \quad \zeta = \frac{c}{2\sqrt{km}}, \quad \bar{f}_n = f_n \frac{D}{U_\infty} = \frac{1}{2\pi} \sqrt{\frac{k}{m}} \frac{D}{U_\infty},
\end{aligned} \tag{5}$$

In these definitions,  $D$  is the diameter of the cylinder,  $U_\infty$  the free stream velocity,  $\rho$  the free stream density,  $U^*$  the reduced velocity,  $Y$  the normalized displacement,  $\tau$  the normalized time, and  $m_d$  is the displaced fluid mass.

### 2.3 Coupling algorithm

A general three-dimensional coupling algorithm is implemented that includes three main modules (Fig. 1): the flow solver, the solid solver, and the load/motion transfer operator that relays relevant analysis parameters between the two solution domains. The conservative load transfer operator imposes the following compatibility conditions, see (Farhat *et al.* 1998)

$$\begin{aligned}
\sigma_S \cdot n = -pn + \sigma_F \quad \text{on } \Gamma, \\
u_S = u_F \quad \text{on } \Gamma,
\end{aligned} \tag{6}$$

where  $\sigma_S$  is the structure stress tensor,  $\sigma_F$  the fluid viscous stress tensor,  $\Gamma$  the fluid/structure interface boundary,  $n$  the normal vector at a point to  $\Gamma$ ,  $u_F$  the ALE displacement field of the fluid, and  $u_S$  the displacement field of the structure.

The coupling starts with an initial flow field solution that provides the surface fluid tractions along the fluid/structure mesh interface. Then, using the conservative load transfer operator, surface tractions are integrated to yield the resultant nodal forces applied on the solid mesh. In this specific problem involving a rigid cylinder, the solid mesh interface can be reduced to the center of mass and loading integrations yield the resultant aerodynamic drag, lift, and moment. The solution of Eq. (3) provides the cylinder displacement, velocity and acceleration at every time step. Second order in time and unconditionally stable  $\beta$ -Newmark algorithm is applied as a direct integration operator within the solid solver. After each time increment, the solid displacement is imposed by the compatibility condition to the nodes of the fluid mesh along the fluid/structure interface, using the load/motion transfer operator. Then, the fluid solver uses this interface motion in the ALE formulation to compute the fluid mesh motion in the entire domain, and then solves the flow field. This loop marches in time until the total analysis duration is achieved.

### 2.4 Initialization and convergence of solution

As a starting point for the computations, the initial flow solution around the body is required. However, at the first time step, there is no converged CFD solution available yet. A common approach to circumvent this problem in fluid-structure interaction problems is to let the flow around the body establish itself completely for shedding vortices to reach their limit cycle. From this point forth, the body starts to move freely. However, a different initialization is used in this study. First, a few time steps are performed in order to get a time-accurate flow established around the fixed cylinder (with an average residual of  $10^{-6}$  at each time step), and then the cylinder is freed

to move. The cylinder oscillates slightly due to a small oscillating fluid loading at early time steps. Since the source of vortex shedding behind the bluff body is flow instabilities, this method helps to reach the limit cycle sooner. This initialization procedure seems to be more realistic, and makes it possible to study the time accurate evolution of the vortices and structural response. In all test cases, the cylinder starts to move from rest, i.e.

$$y_{t=0} = y_0 \text{ and } \dot{y}_{t=0} = 0 \tag{7}$$

It should be noted that we do not focus on the hysteresis response of the cylinder, which happens when the free stream velocity increases or decreases during the simulation.

The selection of the appropriate time step is important in time accurate solutions, and it is required to be computed based on the lowest physical time scale present in the problem. The shedding frequency of the oscillating cylinder ( $f_c$ ) and natural frequency of the structure ( $f_n$ ) are the two important frequencies governing the time scales. At the beginning of the computations,  $f_c$  is unknown; however, generally the frequency ratio of the oscillating cylinder ( $f^* = f_c / f_n$ ) is limited by either the shedding frequency ratio of the fixed cylinder ( $f_s / f_n$ ), or the lock-in frequency ratio (see Fig. 2). The lock-in frequency ratio is generally less than 1.5, and the shedding frequency of the fixed cylinder is computed from an estimated Strouhal number (St) at each Reynolds number (see e.g., (Fey *et al.* 1998) for Re-St functionality). Thus, the time step is computed by dividing one complete shedding or fundamental period, whichever is smaller, by a reasonably large number, say 500, which provides a suitable response resolution on one hand, and, on the other hand, justifies the constant load assumption at each time step. Usually, this time step satisfies the stability criterion of the ALE formulation as well. Thus, Eq. (8) is used to compute the time step.

$$dt = 0.002 T, \quad T = \min\left(\frac{1}{f_s}, \frac{1}{f_n}\right), \quad f_s = St \frac{u_\infty}{D}, \quad St = St\left(\frac{1}{\sqrt{Re}}\right) \tag{8}$$

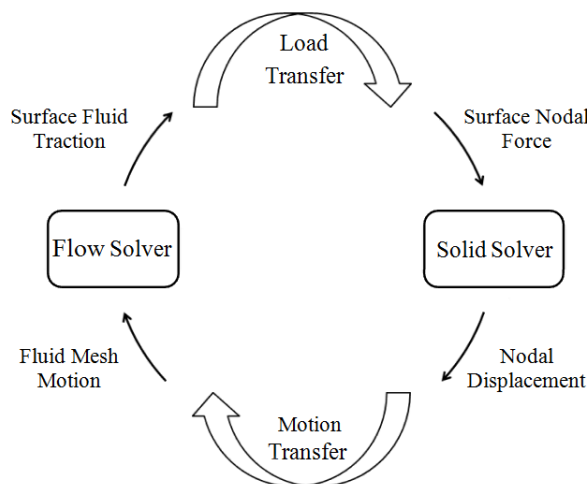


Fig. 1 Global coupling and FSI (fluid-structure interaction) framework

At each time step, a sufficient number of Newton iterations are performed to reach a time accurate solution. Thus, the unsteady residuals of the flow field and turbulence model are reduced by a minimum of three orders at each time step, keeping the average of residuals less than  $10^{-6}$  at all times.

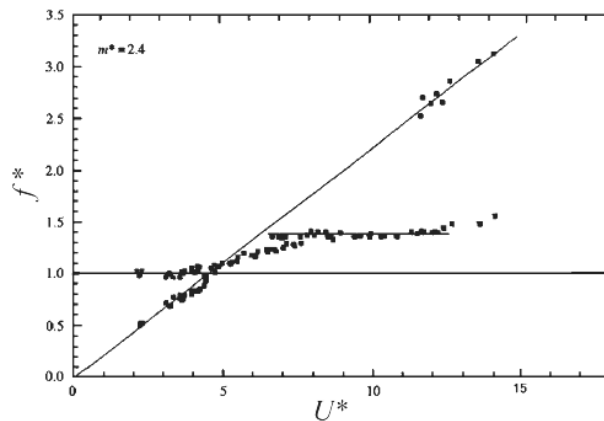


Fig. 2 Frequency response versus reduced velocity of the oscillating cylinder, inclined solid line is the shedding frequency ratio of a fixed cylinder (Williamson *et al.* 2004)

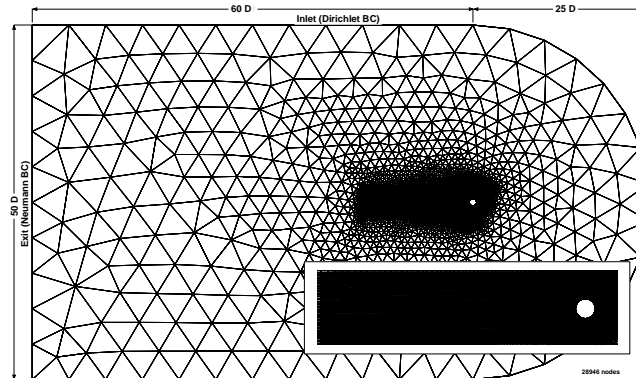


Fig. 3 Spatial grid, dimensions, and boundary conditions

### 2.5 Spatial grid and grid independence

Fig. 3 shows the spatial grid, type of boundary conditions, and dimensions used for the fluid domain model. In this hybrid mesh, an O-grid is used around the cylinder, and the first node off the wall is placed at  $y^+ < 1$  and 5 to 8 nodes are placed at  $y^+ < 10$  to thoroughly capture the boundary layer. In order to capture the details of the near wake, a high resolution structured grid is used within 15D behind the cylinder; an unstructured triangular grid is applied everywhere else. The total number of node is 28946 in which 200 nodes are placed on the cylinder, 60% of the nodes are placed within 4D of the cylinder, and the 15D near wake region has 30% of the total nodes. As the

Mach number is quite low, far field boundaries are placed far enough in order to avoid boundary reflection interferences with the numerical solution. It should be noted that the grid is extruded normal to the plane and periodic boundary condition is applied accordingly. In order to perform a grid independence study, by keeping the time step constant, the grid is refined two times by a factor of 1.5 while keeping the same node ratios in different regions as mentioned above. A FSI solution at Reynolds 8000 over a freely vibrating cylinder was performed for the study and the results are summarized in Table 1. The difference in displacements between the employed grid and the finest grid is less than 3%. Thus the grid presented with 28946 nodes is used throughout the study.

Table 1 Displacement using different grids, Re = 8000

Grid (number of nodes)	$Y_{\max}/D$	Diff. % w.r.t. employed grid
28946	0.504	-
41204	0.494	2
64578	0.490	3

### 3. Numerical Results

In this section, numerical results for a rigid cylinder with low mass-damping are presented for different reduced velocities. In order to compare the results with other published studies, the structural parameters and Reynolds number range correspond to those of an experimental study performed by Khalak *et al.* (1996) and a numerical study done by Guilmineau *et al.* (2004). Hence, a mass ratio of 2.4, a mass-damping ratio of 0.013 and a Reynolds number range of 975-14923, representing a reduced velocity range of 1.124-17.21, are chosen. For all Reynolds numbers, the same structural damping is applied; however, it should be noted that the total damping is composed of the structural and aerodynamic damping. The aerodynamic damping is directly and naturally imposed by flow solution. Hence, the total damping is controlled by flow solution.

Fig. 4 shows the normalized displacement of the cylinder versus the normalized time for different reduced velocities. In these figures, the oscillations start with very small amplitudes, and as time passes, the amplitude increases until it reaches its limit cycle value. The limit cycle amplitude is unique for most of the cases; however, for some reduced velocities, e.g., at  $U^* = 2.883$  and to some extent also at  $U^* = 3.460$ , the limit cycle amplitude beats periodically. This beating behavior in the synchronization (or transition) region is in agreement with the experimental studies of Brika *et al.* (1993). The onset of relatively large oscillations differs with reduced velocity. For  $Re < 1500$  and  $Re \gtrsim 9000$ , corresponding to the head of the initial excitation branch and the tail of the lower branch, respectively, large oscillations start at around  $\tau = 100-150$ ; while, for  $1500 < Re < 9000$ , which includes the transition regions and the upper branch, instabilities become noticeable quite earlier at around  $\tau = 40-50$ .

A close investigation of Fig. 4 shows that within the initial excitation and lower branches, oscillations are of regular bell shape type with one dominant frequency, but inside the upper branch, varying amplitude and beating behavior can be seen. At low reduced velocities, amplitudes are very small (e.g., 0.013 at  $U^* = 1.124$ ), but as velocity increases, the amplitude amplifies dramatically. In the initial-upper transition region, oscillations do not stabilize at a constant value. For instance, at  $U^* = 2.883$ , the amplitude changes between 0.15 and 0.35 (see Fig. 4 and scatter

lines in Fig. 6 ). The amplitude increases through the upper branch and reaches a limit value; however, in this region large displacements start with an overshoot. By further increasing  $U^*$ , the amplitude decreases rapidly until the beginning of the lower branch at  $U^* \sim 6.4$  where the decrease rate is reduced. At  $U^* \sim 9$ , the amplitude decreases rapidly until  $U^* = 12$  where it reaches the small value of 0.034: from this point forth, the change of amplitude with reduced velocity is negligible. Similar to the initial branch, the response of the cylinder in the lower branch is regular and only one dominant frequency is notable.

In Fig. 5, the power spectral density (PSD) estimates for various Reynolds numbers representing the frequency response of the cylinder in different branches, are plotted. In the initial branch, e.g., Re 1500, the PSD of the vertical displacement shows one dominant frequency at 4.78 Hz which is equivalent to the frequency ratio of 0.39, this compares well with the experimental data of Khalak *et al.* (1999). By increasing the reduced velocity and reaching the initial-upper transition region, the PSD becomes broader. For instance at Re 2500, at least two distinct peaks with almost equivalent strengths exist, demonstrating the beating behavior. In the upper branch, at Re 3911 for instance, Fig. 5 demonstrates a single dominant frequency as observed by Khalak *et al.* (1999). In the lower branch, at higher Reynolds numbers such as 7310 and 12000, the shedding returns to a single dominant frequency.

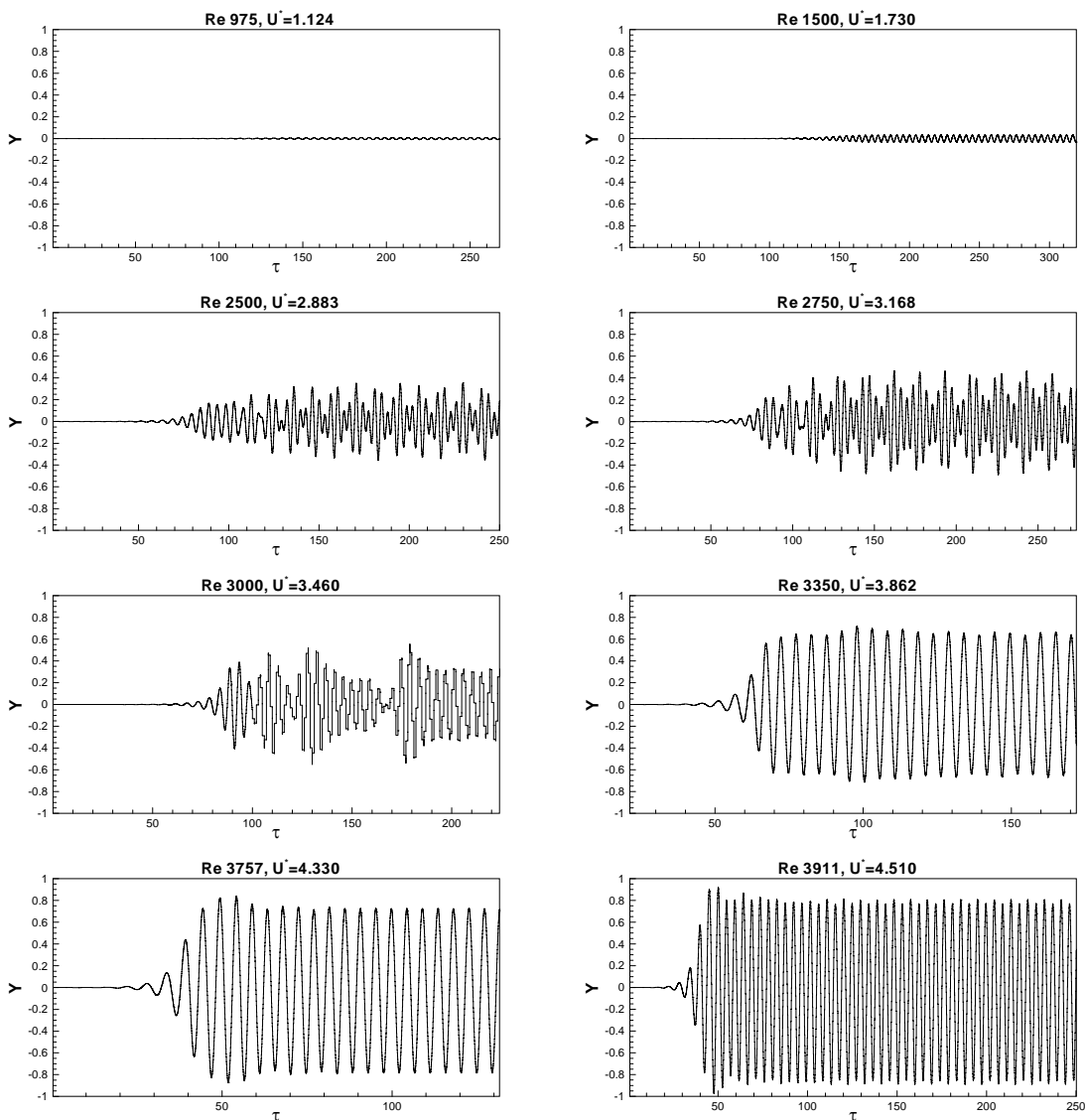
The normalized amplitude of displacements at their limit cycle versus reduced velocity is presented in Fig. 6. In this figure, vertical bars are used to show the range of varying amplitude in the limit cycle, and where the large displacements start with an overshoot. Also in the same figure, the experimental results of Khalak *et al.* (1996) are included for comparison. The maximum computed amplitude happens at  $U^* = 4.510$ . At this reduced velocity, large displacements start with an overshoot of 0.94, and then the oscillations end up at the limit cycle amplitude of 0.83. These values are lower than the experimental value of 0.96. In the numerical study of Guilmineau *et al.* (2004), a maximum amplitude of 0.98 is reported at  $U^* = 4.510$ , with increasing velocity initial condition. Considering the different initial condition used in this study, the predicted maximum amplitude and the overall trend of the results are deemed satisfactory and show agreement with the experiment. The computed amplitudes in the initial and lower branches consistently agree with the experiment. Moreover, the upper branch results are encouraging. It seems that employing greater concentration of points around the cylinder and in the near wake region has made it possible to capture the upper branch while the upper branch had not been captured by other published numerical studies, see e.g., (Guilmineau *et al.* 2004, Pan *et al.* 2007).

In Fig. 7, the frequency ratio versus the reduced velocity is compared with the experimental results. The computed frequency follows the experimental results everywhere, except in the tail of the lower branch where the amplitude of oscillations is very small and the frequency is high. In fact, numerical studies suffer from predicting accurate shedding frequency at high Reynolds numbers. Even in the case of the fixed cylinder, the numerical shedding frequency at high Reynolds numbers is lower than the experimental values. This difference for  $U^* > 12$  is also reported in other computational studies. In this region, the cylinder experiences very small oscillations; therefore, the importance of the frequency ratio is secondary. Several studies show the presence of the lock-in phenomenon in vortex-induced vibrations in which the structural motion dominates the shedding development, then the shedding frequency shifts to the structural

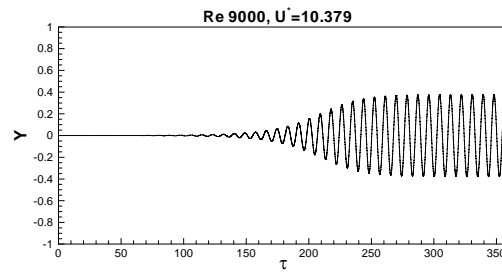
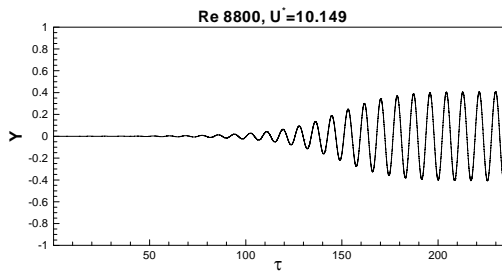
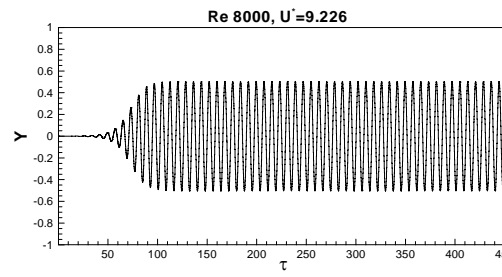
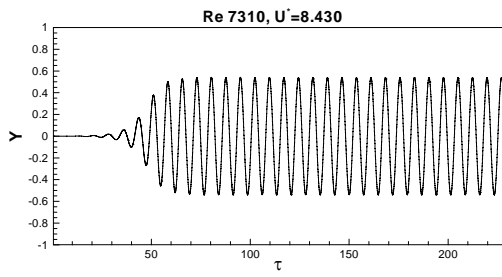
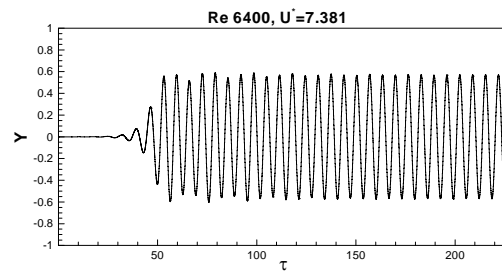
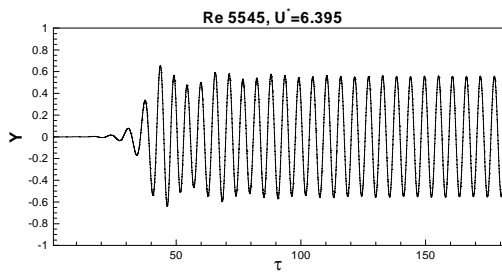
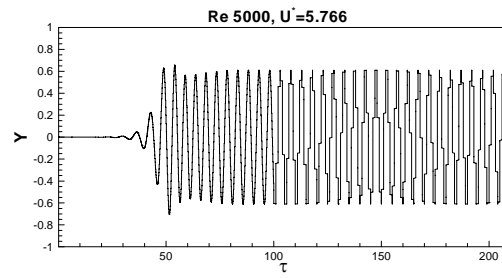
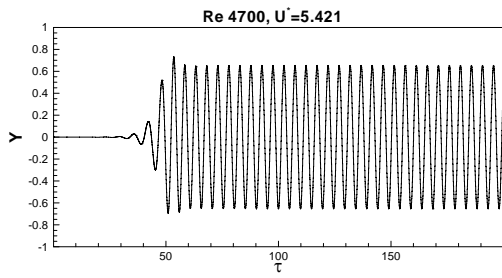
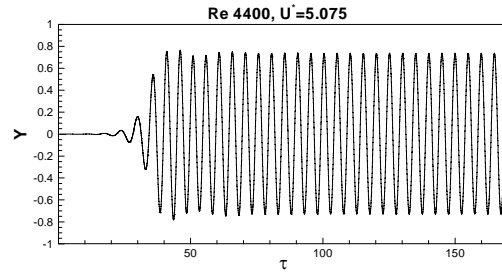
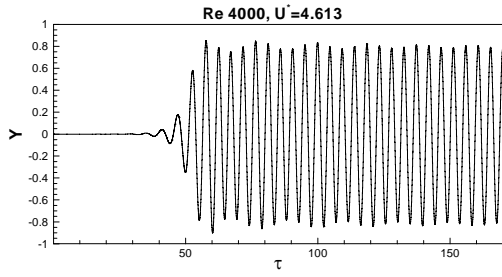
---

∴ The free stream velocity is increased from an initial value gradually up to a target value while the cylinder oscillates.

frequency, i.e.,  $f_s \sim f_n \sim f_c$ , see, e.g., (Brika *et al.* 1993, Blackburn *et al.* 1996, Williamson *et al.* 2004). It is shown experimentally that for high mass ratios, the frequency ratio  $f^*$  is close to unity; however, as the mass ratio decreases, the frequency ratio departs from unity and reaches a higher value. Fig. 7 shows the frequency ratio of 1.2 within the lock-in region,  $U^* = 4.6 - 12$ , which is lower than the experimental value of 1.4 reported by Khalak *et al.* (1999). Close investigation of the frequency response and time history of the displacements (Fig. 4) shows that the onset of the large oscillations happens within the lock-in region. Past the lock-in region, the amplitude of oscillations drops to a very small value and remains unchanged.



Continued



Continued

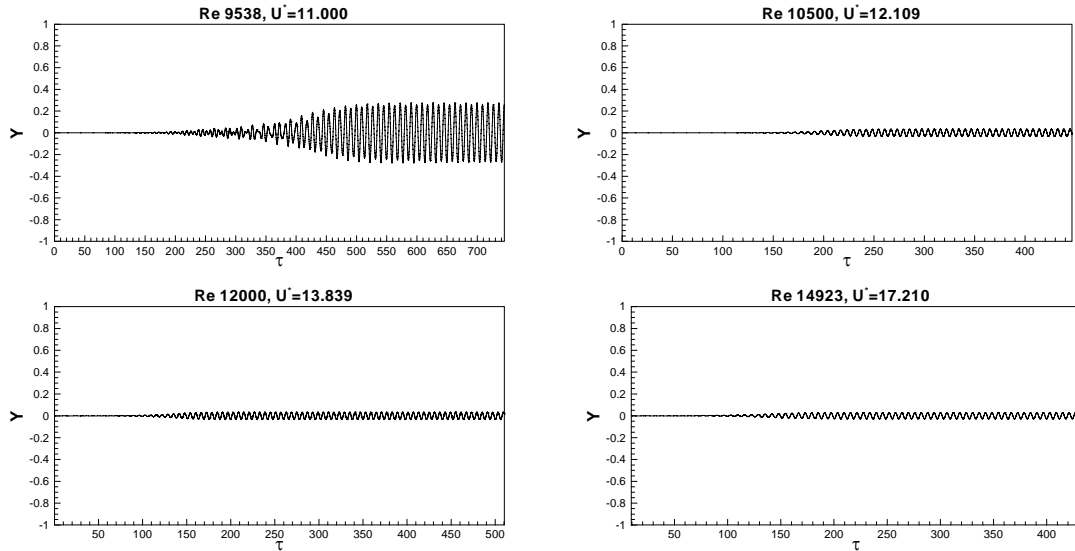
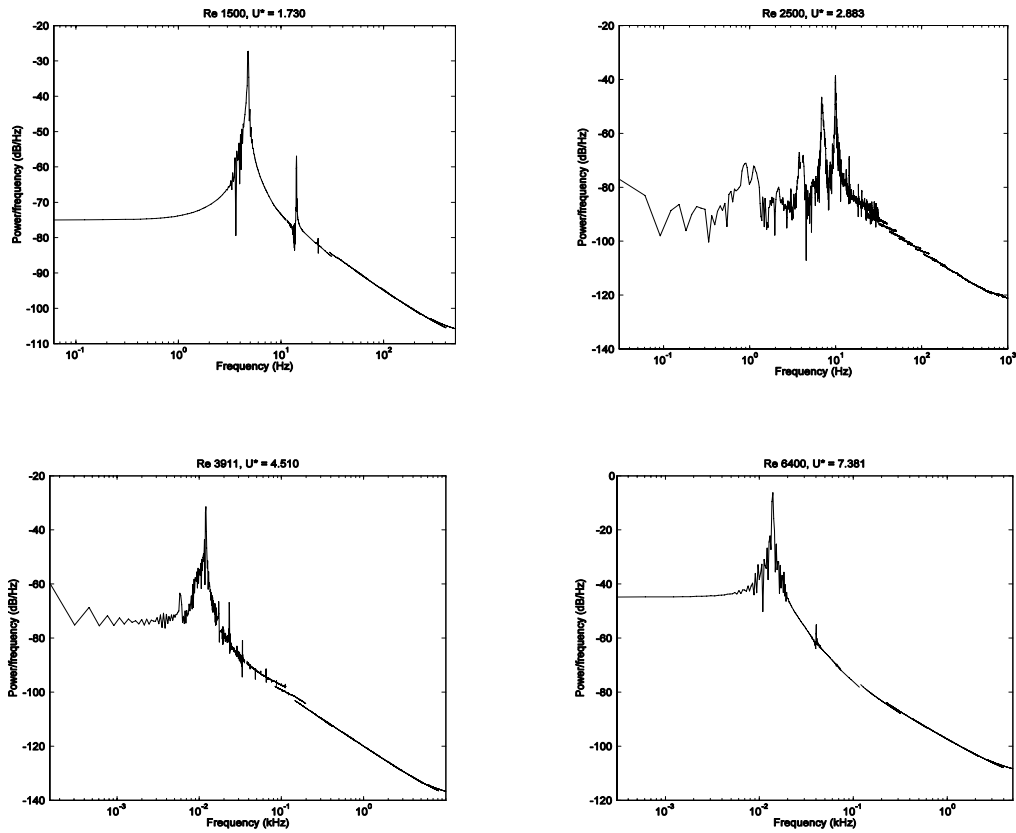


Fig. 4 Normalized time history of vertical displacement of the cylinder ( $m^* = 2.4$ ,  $m^* \zeta = 1.3 \times 10^{-2}$ ) at various reduced velocities



Continued

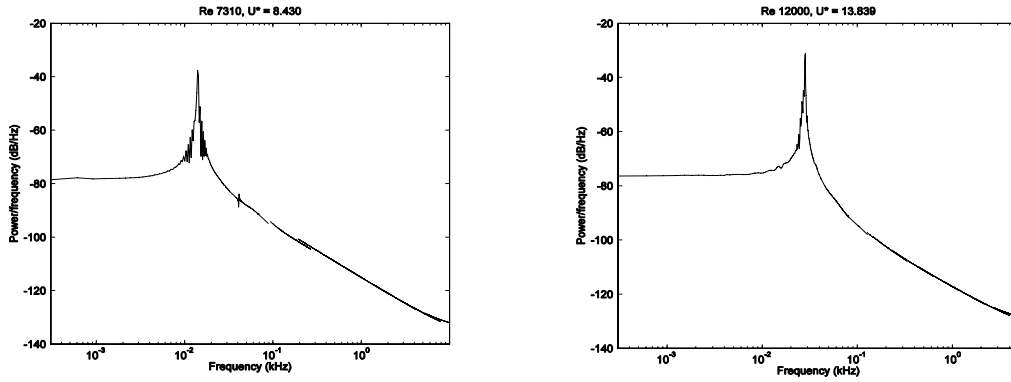


Fig. 5 Periodogram Power Spectral Density (PSD) estimate of the vertical displacements at various reduced velocities

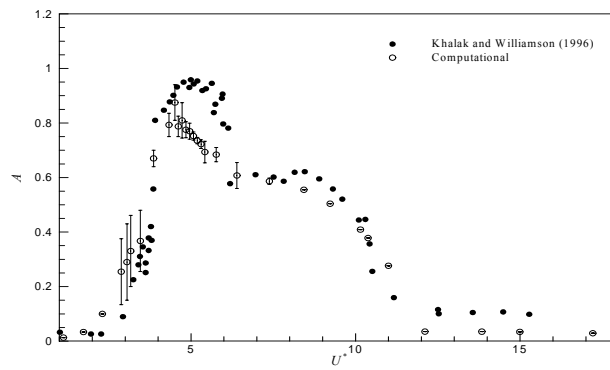


Fig. 6 Limit-cycle amplitude versus reduced velocity, ( $m^* = 2.4$ ,  $m^* \zeta = 1.3 \times 10^{-2}$ ); scatter bars show varying amplitudes obtained by FSI analysis

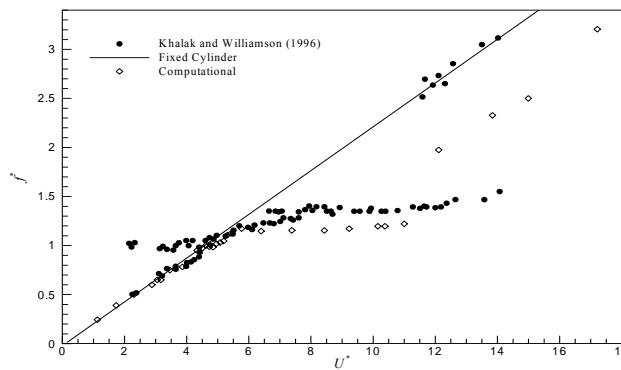
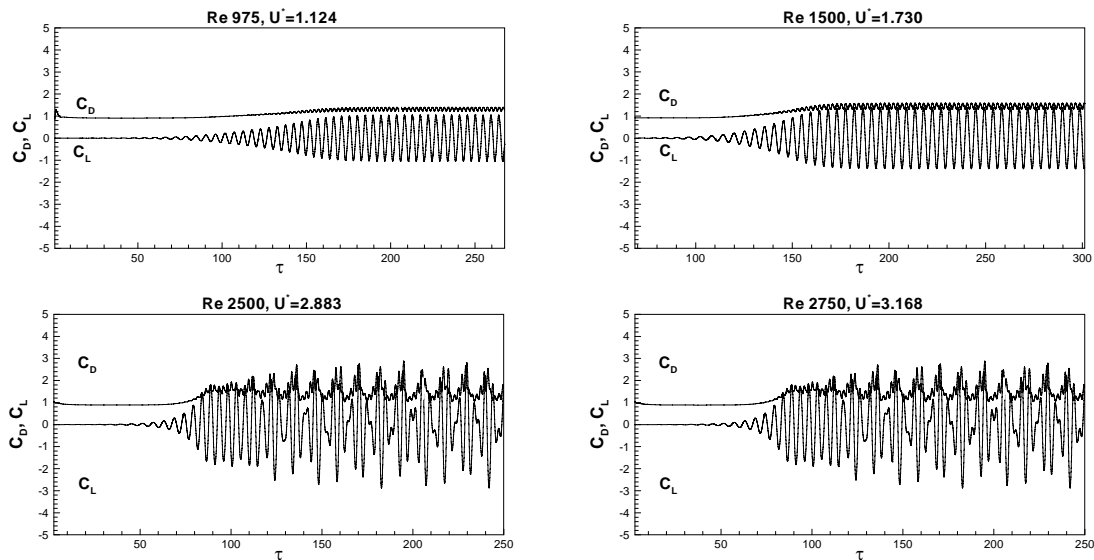


Fig. 7 Frequency ratio versus reduced velocity, ( $m^* = 2.4$ ,  $m^* \zeta = 1.3 \times 10^{-2}$ )

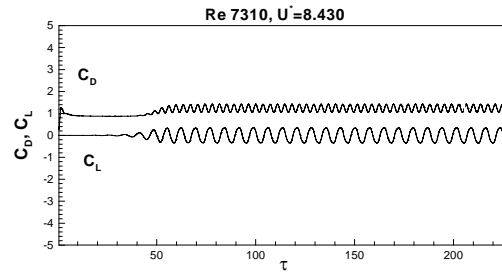
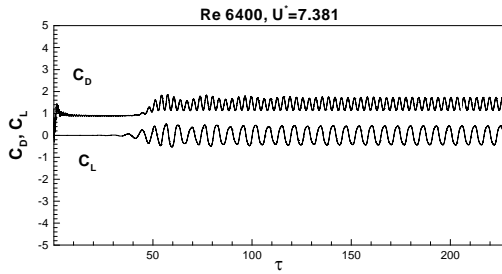
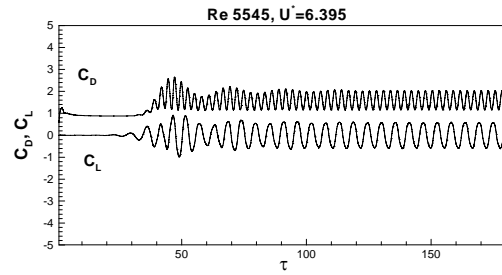
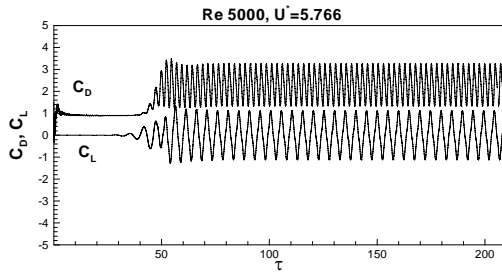
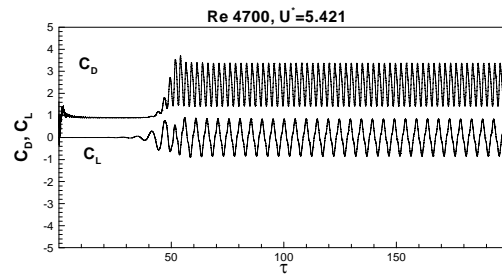
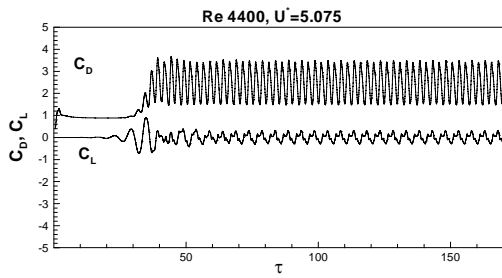
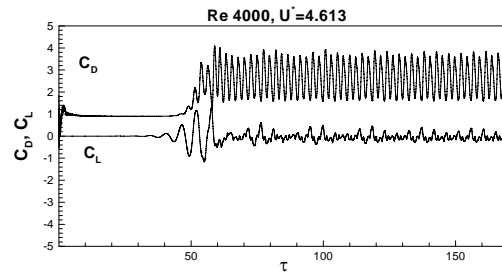
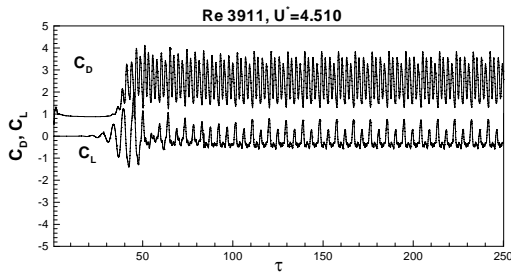
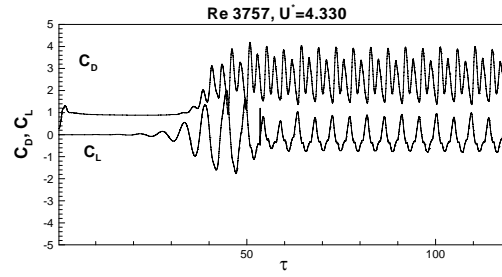
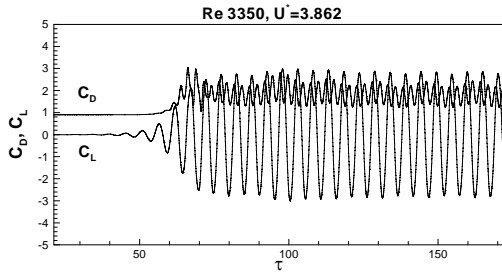
Fig. 8 presents the loading (lift and drag coefficients) history for different reduced velocities. At low reduced velocities, the fluctuations of the drag coefficient are smaller than those of the lift coefficient, but by increasing the reduced velocity, these fluctuations become of the same order until the cylinder reaches its maximum amplitude. From this point forth, the fluctuations of drag become greater than lift fluctuations, and the mean drag coefficient reaches its maximum value at maximum amplitude. As exposed area of cylinder reaches its maximum at highest amplitude, coincidence of the maximum amplitude and maximum drag is predictable. By further increasing the reduced velocity, fluctuations of both the lift and drag coefficients decrease and reach a small value at high reduced velocities. An interesting observation is the loading history at the initial-upper transition region (Fig. 8,  $U^* = 2.883-4.330$ ). In this region, similar to the displacement response, the amplitude of the loading varies with time and the regular loading seen in other regions is not observed.

Fig. 9 shows the effect of transverse oscillations on the drag coefficient. In this figure, the computed mean and maximum drag coefficients are plotted versus reduced velocity. As the area of the cylinder exposed to the flow increases with amplitude, the cylinder is expected to experience a greater drag force as amplitude increases. As expected, results show that both the mean and maximum drag coefficients reach their peak value at maximum amplitude. The peak drag force on the oscillating cylinder is larger than on a fixed cylinder; in the current case, the peak mean drag is three times larger than the drag coefficient of a similar fixed cylinder.

The phase angle,  $\Phi$ , between the lift force and the displacement response, versus the reduced velocity is plotted in Fig. 10. For  $U^* < U^*_{max\ amplitude}$ , the phase angle is near zero while, after passing the maximum amplitude, the phase angle jumps to around +185 degrees.



Continued



Continued

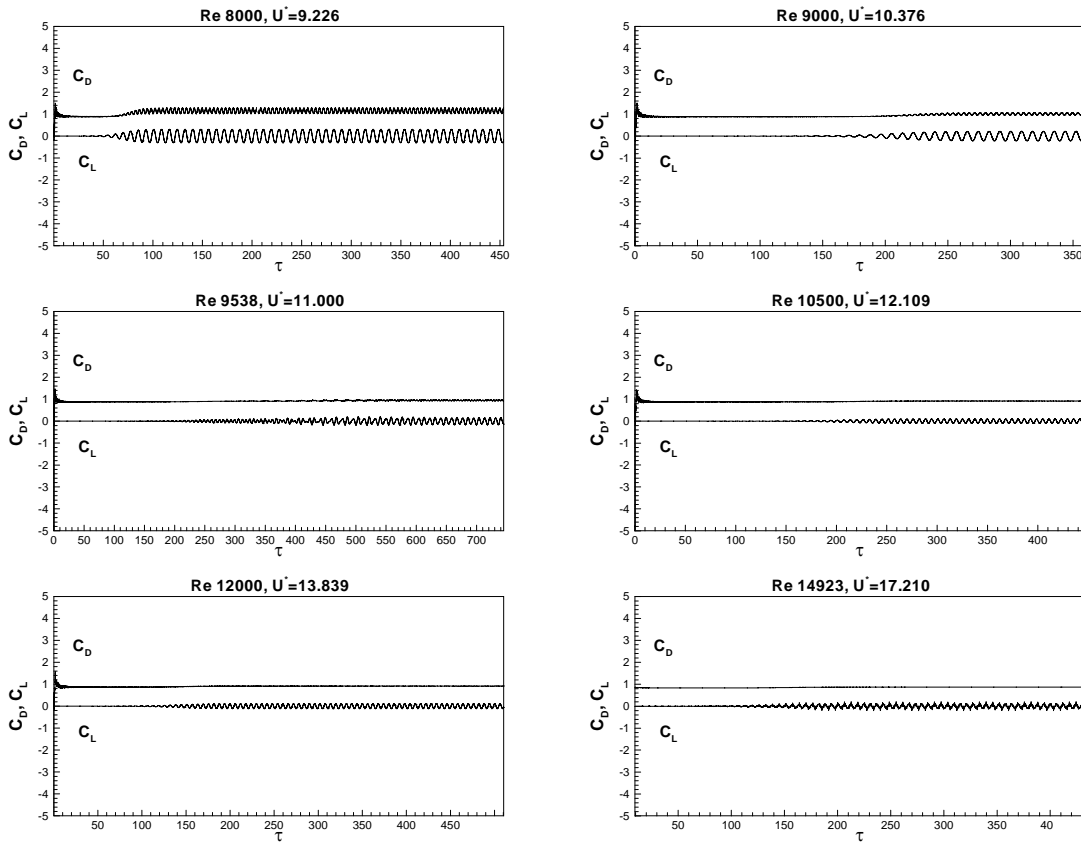


Fig. 8 Normalized time history of loading over the vibrating cylinder ( $m^* = 2.4$ ,  $m^* \zeta = 1.3 \times 10^{-2}$ ) at various reduced velocities

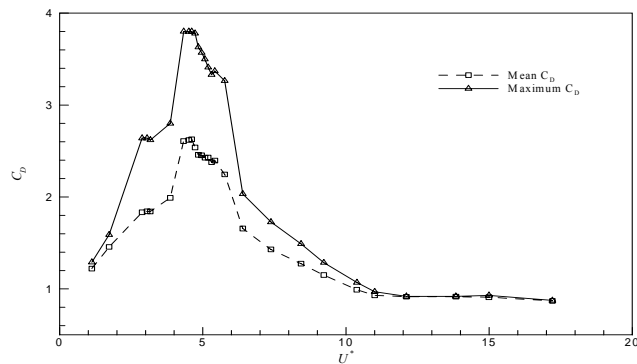


Fig. 9 Mean and maximum drag coefficients versus reduced velocity of oscillating cylinder, ( $m^* = 2.4$ ,  $m^* \zeta = 1.3 \times 10^{-2}$ )

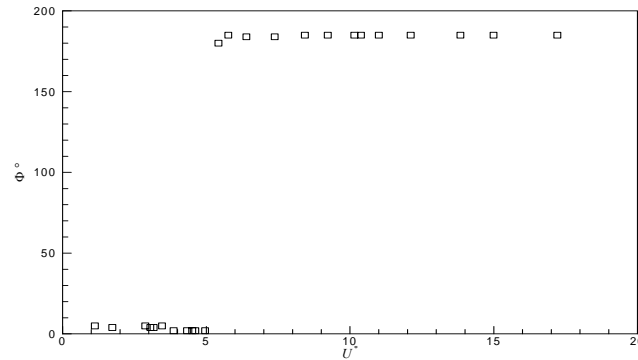
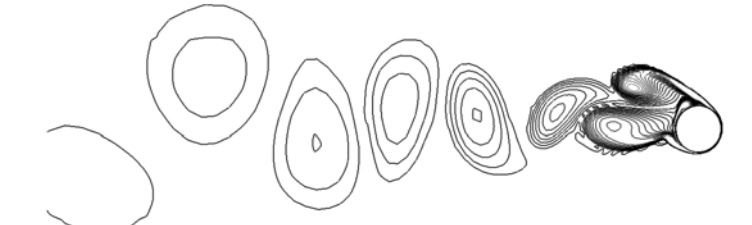
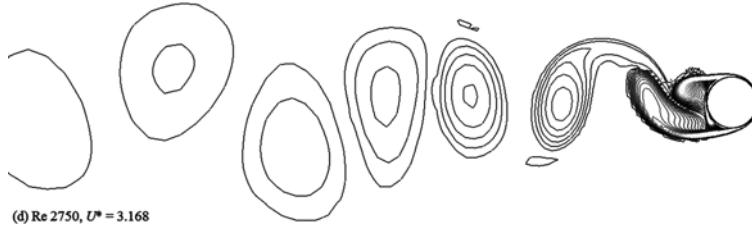
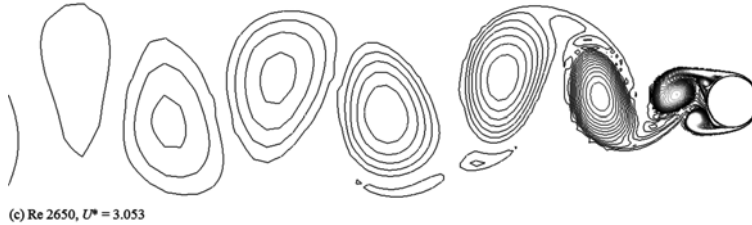
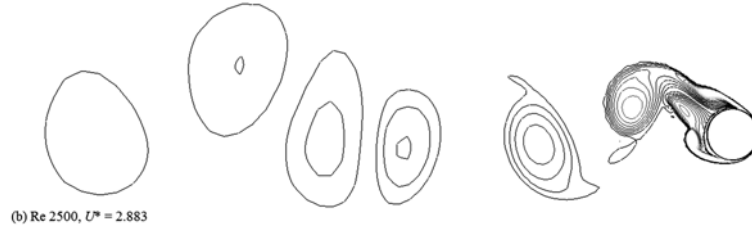
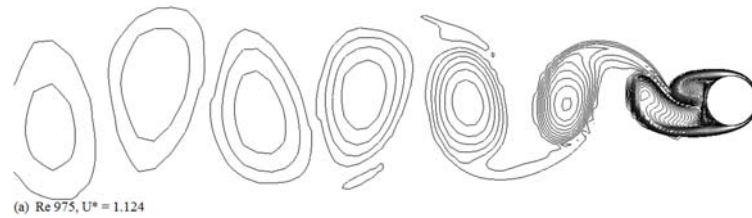


Fig. 10 Phase angle versus reduced velocity of oscillating cylinder, ( $m^* = 2.4$ ,  $m^* \zeta = 1.3 \times 10^{-2}$ )

The vortex shedding mode and structure of the vortices alter the aerodynamic loading and damping of the cylinder. Consequently, this affects the response of the cylinder. On the other hand, the frequency and amplitude of the oscillations changes the shedding mode and structure of the vortices. Thus, studying the structure of the vortices and shedding modes facilitates to understand the connection between the shedding modes and the structural response at different Reynolds numbers. Following the interpretation of Williamson *et al.* (1988), flow visualization behind the oscillating cylinder is explored in Fig. 11. In the literature, 2S and 2P vortex shedding modes are reported for this problem, see e.g., (Brika *et al.* 1993). As illustrated schematically in Fig. 12, in 2S mode, two single vortices are fed into the downstream per shedding cycle and in 2P mode, two vortex pairs appear per shedding cycle. Fig. 11 shows the vortex pattern behind the oscillating cylinder for the studied incident flow conditions. At low reduced velocities, the flow has enough time to generate repeatable vortex patterns, and small amplitudes keep the shedding area narrow, thus a pure periodic 2S mode appears as illustrated in Fig. 11(a). By increasing the reduced velocity and reaching the initial-upper transition region, the amplitude beats, and the required time and space to complete a full 2P or 2S shedding cycle is not available. Therefore, the mode alternates between 2S and 2P; see Fig. 11(b)-(e). The mode switching in this region is related to the previously mentioned beating behavior in the displacement response and loading. By increasing the reduced velocity and reaching the upper branch region, the vortex street keeps expanding, and the 2P mode becomes dominant; Fig. 11(f)-(j). This change in shedding mode coincides with the phase angle shift from 0 to +180 degrees. The widest vortex street appears in the upper-lower transition where the frequency ratio jumps at the end of the lock-in region (see Fig. 7). By further increasing the reduced velocity, the vortex street becomes narrower, see Fig. 11(k), and it seems that the vortex pattern tends to return to 2S mode afterward. The vortex structures in different regions and alternation of the shedding modes in the transition regions are in agreement with the experiments of Brika *et al.* (1993) and Williamson *et al.* (1988).



Continued

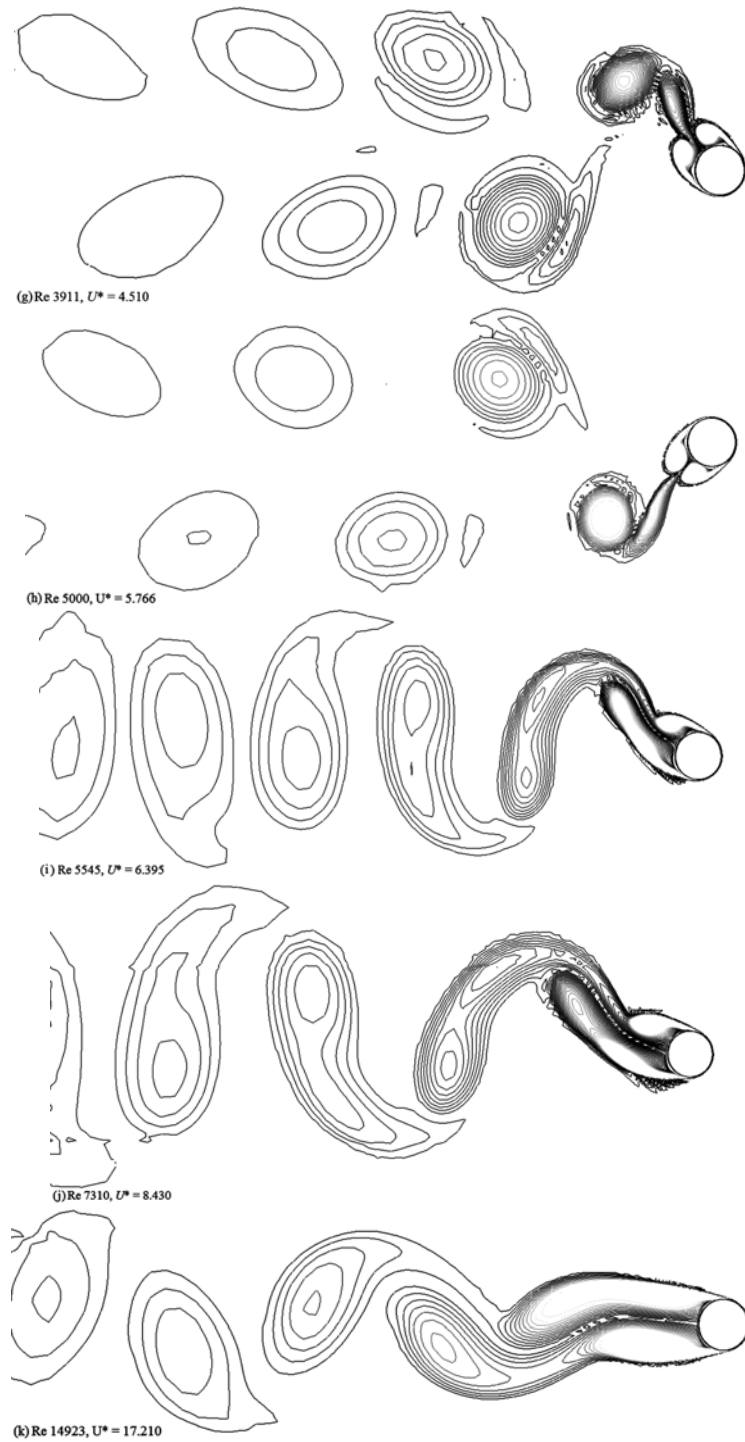


Fig. 11 Instantaneous vorticity contours for different Reynolds numbers of the oscillating cylinder, ( $m^* = 2.4$ ,  $m^* \zeta = 1.3 \times 10^{-2}$ )

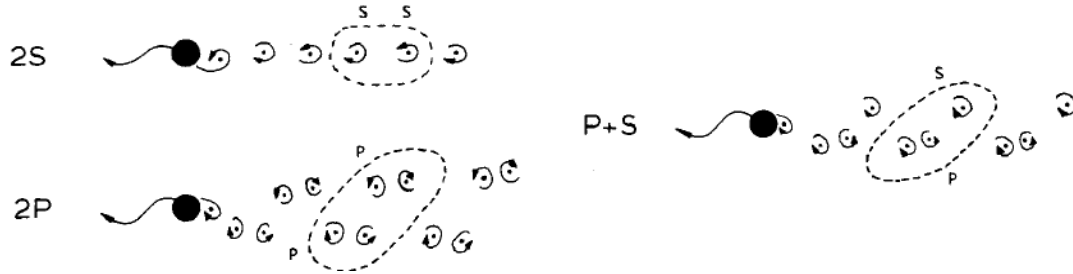


Fig. 12 Sketches of vortex shedding patterns, (Williamson *et al.* 1988)

In Fig. 13, the computational results are summarized in one graph to facilitate analyzing different aspects of VIV response and their effects on each other. A first observation is the coincidence of the maximum drag force and the maximum amplitude with the shift of phase angle from 0 to 180 degrees. At this point, the vortex shedding mode switches to 2P, as well. The lock-in region, where the frequency ratio reaches almost a constant value, starts at the upper-lower branch border, and ends when the displacement amplitude drops to a small value. At this point, the drag force and the amplitude reach their lowest values, and the frequency ratio starts to increase.

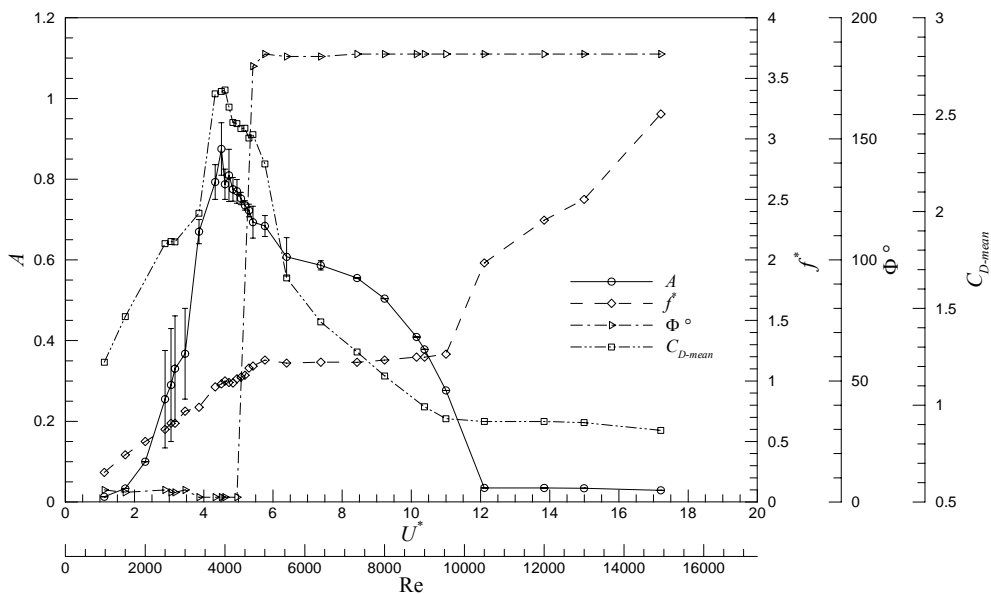


Fig. 13 Summary of computational results

#### 4. Conclusions

In this paper, the transverse vortex-induced vibration of a circular cylinder with low

mass-damping is numerically studied using URANS with the Spalart-Allmaras turbulence model in a fluid-structure interaction analysis. In the absence of DNS and LES models for moderate Reynolds numbers applications, the present cost-effective numerical methodology shows that URANS models can be efficiently used to predict the salient features of the flow around freely vibrating bluff bodies including the near wake structure, the shedding modes, and unsteady loading. Moreover, the numerical results including structural and frequency responses, vortex shedding modes, fluid force, phase angle, and history of developing large displacements, are compared with experiments and show very good agreement. More importantly, the numerical results show an encouraging improvement over previous studies in capturing the upper branch of the response. Although calculated amplitudes in the upper branch are slightly lower than the experimental values, in the other branches, the amplitudes are predicted correctly. Moreover, flow visualization reveals an association of the 2S mode with the initial branch, of the 2P mode with the upper and lower branches, and of the mode switching within the initial-upper transition region. This mode association with different response branches had been previously reported in experimental studies by Brika *et al.* (1993).

## Acknowledgements

The authors would like to thank Le Fonds québécois de la recherche sur la nature et les technologies for its generous support of the present research.

## References

- Bearman, P.W. (1984), "Vortex shedding from oscillating bluff bodies", *Annu. Rev. Fluid Mech.*, **16**(1), 195-222.
- Blackburn, H. and Henderson, R. (1996), "Lock-in behavior in simulated vortex-induced vibration", *Exp. Therm. Fluid Sci.*, **12**(2), 184-189.
- Blackburn, H.M., Govardhan, R.N. and Williamson, C.H.K. (2001), "A complementary numerical and physical investigation of vortex-induced vibration", *J. Fluid. Struct.*, **15**(3-4), 481-488.
- Blackburn, H.M. and Karniadakis, G.E. (1993). "Two- and Three-dimensional simulations of vortex-induced vibration of a circular cylinder", *Proceedings of the 3rd (1993) International Offshore and Polar Engineering Conference, Part 3 (of 4), June 6, 1993 - June 11, 1993*, Singapore.
- Blevins, R.D. (1994), *Flow-induced vibration*, Krieger, Malabar, Florida.
- Brika, D. and Laneville, A. (1993), "Vortex-induced vibrations of a long flexible circular cylinder", *J. Fluid Mech. Digital Archive*, **250**(1), 481-508.
- Farhat, C., Lesoinne, M. and Le Tallec, P. (1998), "Load and motion transfer algorithms for fluid/structure interaction problems with non-matching discrete interfaces: Momentum and energy conservation, optimal discretization and application to aeroelasticity", *Comput. Meth. Appl. Mech. Eng.*, **157**(1-2), 95-114.
- Feng, C.C. (1968), *The measurements of vortex-induced effects in flow past stationary and oscillating circular and D-section cylinder*, University of British Columbia, Vancouver, B.C., Canada.
- Fey, U., Konig, M. and Eckelmann, H. (1998), "A new Strouhal--Reynolds-number relationship for the circular cylinder in the range  $47 \leq Re \leq 2 \times 10^5$ ", *Phys. Fluid.*, **10**(7), 1547-1549.
- Govardhan, R. and Williamson, C.H.K. (2000), "Modes of vortex formation and frequency response of a freely vibrating cylinder", *J. Fluid Mech.*, **420**(Copyright 2000, IEE), 85-130.

- Guilmineau, E. and Queutey, P. (2004), "Numerical simulation of vortex-induced vibration of a circular cylinder with low mass-damping in a turbulent flow", *J. Fluid. Struct.*, **19**(4), 449-466.
- Habashi, W.G. (2009), "Advances in CFD for in-flight icing simulation", *J. Japan Soc. Fluid Mech.*, **28**(2), 99-118.
- Habashi, W.G., Aubé, M., Baruzzi, G., Morency, F., Tran, P. and Narramore, J.C. (2004), *FENSAP-ICE: A full-3d in-flight icing simulation system for aircraft, rotorcraft and UAVS*, Yokohama, Japan
- Khalak, A. and Williamson, C.H.K. (1996), "Dynamics of a hydroelastic cylinder with very low mass and damping", *J. Fluid. Struct.*, **10**(5), 455-472.
- Khalak, A. and Williamson, C.H.K. (1999), "Motions, forces and mode transitions in vortex-induced vibrations at low mass-damping", *J. Fluid. Struct.*, **13**(7-8), 813-851.
- Newman, D.J. and Karniadakis, G.E. (1997), "A direct numerical simulation study of flow past a freely vibrating cable", *J. Fluid Mech.*, **344**, 95-136.
- Pan, Z.Y., Cui, W.C. and Miao, Q.M. (2007), "Numerical simulation of vortex-induced vibration of a circular cylinder at low mass-damping using RANS code", *J. Fluid. Struct.*, **23**(1), 23-37.
- Pomarède, M., Longatte, E. and Sigrist, J.F. (2010), "Numerical simulation of an elementary Vortex-Induced-Vibration problem by using fully-coupled fluid solid system computation", *Int. J. Multiphysics*, **4**(3), 273-291.
- Sarpkaya, T. (1979), "Vortex-induced oscillations: a selective review", *J. Appl. Mech.*, **46**(2), 241-258.
- Sarpkaya, T. (2004), "A critical review of the intrinsic nature of vortex-induced vibrations", *J. Fluid. Struct.*, **19**(4), 389-447.
- Spalart, P.R. and Allmaras, S.R. (1992), "A one-equation turbulence model for aerodynamic flows", *AIAA-Paper 92-0439*.
- Williamson, C.H.K. and Govardhan, R. (2004), "Vortex-induced vibrations", *Annu. Rev. Fluid Mech.*, **36**(1), 413-455.
- Williamson, C.H.K. and Roshko, A. (1988), "Vortex formation in the wake of an oscillating cylinder", *J. Fluid. Struct.*, **2**(4), 355-381.